

PAPER • OPEN ACCESS

# Effect of coating few-layer WS<sub>2</sub> on the Raman spectra and whispering gallery modes of a microbottle resonator

To cite this article: Shubhayan Bhattacharya *et al* 2020 *J. Opt.* **22** 105003

View the [article online](#) for updates and enhancements.

## You may also like

- [OGLE-ING THE MAGELLANIC SYSTEM: STELLAR POPULATIONS IN THE MAGELLANIC BRIDGE](#)  
D. M. Skowron, A. M. Jacyszyn, A. Udalski et al.
- [Spatiotemporal Interpolation Methods for Solar Event Trajectories](#)  
Soukaina Filali Boubrahimi, Berkay Aydin, Michael A. Schuh et al.
- [Simulation and computational study of U-mold membrane components by CFD multiphase flow Euler model](#)  
Chunqing Li, Ming Zhang, Tao Wang et al.

# Effect of coating few-layer WS<sub>2</sub> on the Raman spectra and whispering gallery modes of a microbottle resonator

Shubhayan Bhattacharya<sup>1</sup> , Aneesh V Veluthandath<sup>1</sup> , C C Huang<sup>2</sup> ,  
Ganapathy Senthil Murugan<sup>2</sup>  and Prem B Bisht<sup>1</sup> 

<sup>1</sup> Department of Physics, Indian Institute of Technology Madras, Chennai 600036, India

<sup>2</sup> Optoelectronics Research Centre, University of Southampton, SO17 1BJ, United Kingdom

E-mail: [bisht@iitm.ac.in](mailto:bisht@iitm.ac.in)

Received 27 April 2020, revised 17 July 2020

Accepted for publication 7 August 2020

Published 3 September 2020



## Abstract

Multi-layered tungsten disulfide (WS<sub>2</sub>) coated silicon/silica (Si/SiO<sub>2</sub>) substrate and SiO<sub>2</sub> micro-bottle resonators (MBRs) have been prepared by van der Waals epitaxy method. Raman spectra of WS<sub>2</sub>-coated MBR show that the out-of-plane Raman mode is sensitive to the polarization of the excitation laser. The quality factor (*Q*) values of the whispering gallery modes (WGMs) in the transmission spectrum of an MBR decrease by 2 orders of magnitude on coating with WS<sub>2</sub>. On coating, a cleaner spectrum is obtained along with a concomitant effect of decrease in the number of lossy modes. Fano resonances as well as Autler-Townes splitting (ATS) was observed for the WGMs in the cleaned transmission spectrum. From the simulations it has been verified that the scattered electric field of the WS<sub>2</sub> flakes contributes to the observation of the Fano resonances and ATS in the coated MBR spectra.

**Keywords:** Raman spectroscopy, 2D materials, microbottle resonators, whispering gallery modes, Fano resonances

(Some figures may appear in colour only in the online journal)

## 1. Introduction

Two dimensional (2D) materials and their heterostructures have attracted considerable attention since the discovery of graphene [1]. The layered transition metal dichalcogenides (TMDCs) [2] fall under the category of 2D materials. These compounds are of the form MX<sub>2</sub> having a structure with a constituent tri layer consisting of a metal (M=Mo, W, Nb) sandwiched between two chalcogen layers (X=S, Se, or Te). These materials exhibit phenomena such as indirect to direct band-gap transitions [3], strong photo- and electro-luminescence [3, 4] and are promising materials for

optoelectronic devices [5]. Integration of TMDCs with optical cavities can lead to phenomena of low threshold lasing [6], enhanced Raman scattering [7] and strong light-matter coupling [8, 9].

One of the actively investigated TMDC is tungsten disulfide (WS<sub>2</sub>). The bulk WS<sub>2</sub> is an indirect band-gap semiconductor with a band gap range of 1.3–1.4 eV depending on its phase [10]. The properties of WS<sub>2</sub> depend on the number of layers. It becomes direct-band gap material for its monolayer that exhibits strong photoluminescence. Nano antenna enhanced light matter interaction has been reported in atomically thin WS<sub>2</sub> [6, 11]. Raman spectroscopy has been used to determine the number of layers in a TMDC [12]. WS<sub>2</sub> exhibits two main Raman-active vibrations, the in-plane E<sub>2g</sub> mode and the out-of-plane A<sub>1g</sub> mode. The A<sub>1g</sub> mode indicates the out-of-plane displacement of S atoms (OC modes) while the E<sub>2g</sub> modes corresponds to the relative motion of W and S atoms (IMC modes) [13]. The frequency difference between the two



Original content from this work may be used under the terms of the [Creative Commons Attribution 4.0 licence](https://creativecommons.org/licenses/by/4.0/). Any further distribution of this work must maintain attribution to the author(s) and the title of the work, journal citation and DOI.

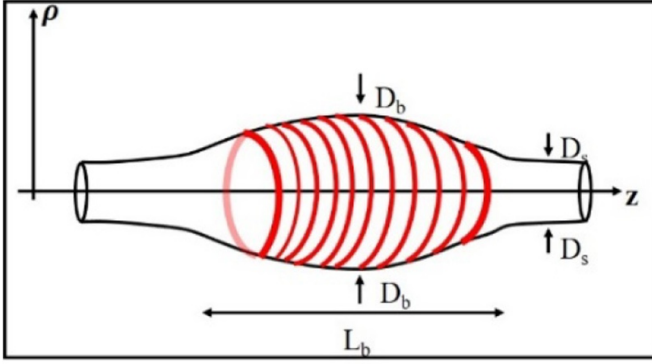


**Figure 1.** Schematic of an MBR.  $D_b$ —bottle diameter,  $L_b$ —length of the MBR and  $D_s$ —stem diameter.

modes increases with the increase in the number of layers and thus can be used to monitor the number of layers in the prepared sample [12].

WS<sub>2</sub> has been integrated with optical microcavities to enhance the strength of light–matter interaction in a fully monolithic cavity with distributed Bragg reflectors [8, 14]. One of the important class of microcavities are whispering gallery mode (WGM) microcavities [15]. WGMs are observed in dielectric microstructures with rotational symmetry such as spheres, rings, and toroids [15–17]. The light is localized due to the total internal reflection in WGMs [15]. These microcavities offer high quality factor (Q-factor) and low mode volume [16] and are sensitive to size, shape and the surrounding refractive index [18]. In contrast to the spherical microcavity [15], the micro-bottle resonators (MBRs) [19] have a highly prolate spheroidal shape and support WGMs that are extended along the  $z$ -axis of the resonator [20]. Figure 1 shows the schematic of an MBR. The outer diameter of the MBR can be fitted with a truncated harmonic oscillator profile:  $D(z) = D_b [1 + (\Delta k z)^2]^{-1/2}$  where  $D_b$  is the diameter at the center of the MBR and  $\Delta k$  is the curvature of the resonator profile. The MBR is characterized by three quantum numbers ( $m, p, q$ ) where  $m$  denotes the azimuthal quantum number or mode number,  $p$  denotes the radial quantum number and  $q$  the axial quantum number.

MBRs have higher axial radii compared to microspheres and hence the axial modes are well separated as shown in figure 2(A). Finite element method (FEM) in COMSOL Multiphysics (5.3a) was used for simulation of electric field distribution of MBR. The electric field distribution of different axial modes ( $q = 1$ –5) for TM<sub>105</sub> mode has been calculated (figure 2(B)).

The spectra of MBRs contain large number of WGMs due to its shape. Cleaning of such spectra to obtain relatively small number of WGMs is essential for the applications in sensors for monitoring a specific WGM. It has been reported that the cleaner spectrum of an MBR can be obtained by changing the diameter of the tapered fiber from 2 to 10  $\mu\text{m}$  [21]. In this paper, the cleaned spectra have been obtained by coating the MBRs with WS<sub>2</sub> flakes. The Q-factor has been found to decrease from  $10^7$  to  $10^5$  in the cleaned spectra.

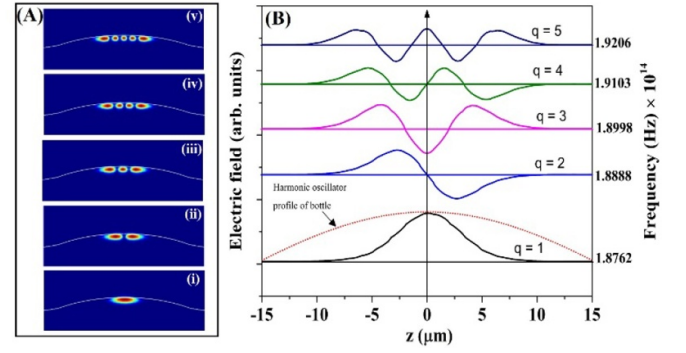


**Figure 2.** (A) Electric field distribution of TM<sub>105</sub> mode for different axial modes  $q = 1$ –5 (i–v) in MBR. (B) The electric field as a function of the axis of the MBR along with the corresponding frequencies. The dotted line shows the fitted truncated harmonic oscillator profile for the MBR in (A) with  $D_b = 19.69 \mu\text{m}$  and  $\Delta k = 0.031 \mu\text{m}^{-1}$ .

The simulations indicate that the interaction of the WGMs of MBRs with the Mie scattering of WS<sub>2</sub> flakes gives rise to the Fano [22–24]—type and electromagnetic induced transparency [25, 26] (EIT)—type resonances as well as the Autler Townes splitting (ATS) in the observed spectra.

The paper is organized as follows. Section 2 gives the experimental details. In section 3.1, WS<sub>2</sub> has been characterized by the techniques of Raman, photoluminescence (PL) and atomic force microscopy (AFM). The effect of polarization on the Raman spectra is also given here. Section 3.2 gives the characterization of the MBR on coating with WS<sub>2</sub>. Observation of Fano resonances in coated MBR is given in section 3.2.2 while section 3.2.3 gives the details of the observed ATS. Conclusions are given in section 4.

## 2. Experimental details

The MBRs used in the present study were prepared by melt and fuse method developed by Murugan *et al* [19]. In brief, in this thermo-mechanical process, two ends of a cleaved fiber are pushed toward each other, heated at the same time thereby they melt and fuse forming bulge shaped structure. WS<sub>2</sub> has been synthesized on fused silica substrate and MBR by van der Waals epitaxy (VdWE) using tungsten hexachloride (WCl<sub>6</sub>) as the precursor to react with hydrogen sulfide (H<sub>2</sub>S) gas [27, 28]. VdWE has number of advantages over the transfer method [29], such as conformal coating on the MBR and substrate and the sizes are typically in 25 mm × 25 mm. For coating the MBRs with WS<sub>2</sub>, the tails of preformed MBRs were affixed on the top surface of a fused silica plate (25 mm × 25 mm × 1 mm) with the help of a high temperature ceramic epoxy (Ceramix TC, FortaFix) and these MBRs were suspended above another fused silica plate (25 mm × 25 mm × 0.5 mm) as the reference sample. This set up (as shown in figure 3(A)) was placed on top of a quartz boat and kept inside the VdWE quartz reactor for WS<sub>2</sub> to be conformally deposited on the MBRs and the reference fused silica substrate.

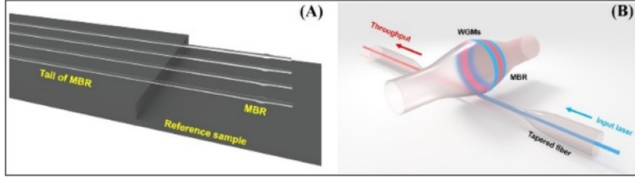


**Figure 3.** (A) Experimental arrangement for coating the MBR. (B) The expended view of the MBR and the tapered fiber geometry used for the MBR characterization.

Raman and PL spectra were recorded using a micro Raman spectrometer (Jobin Yvon, Labram HR 800) with a resolution of  $<1 \text{ cm}^{-1}$  at the excitation wavelength of 488 nm (Argon ion laser). Polarization dependent measurements were carried out by using a half wave ( $\lambda/2$ ) plate at the excitation side and an analyzer on the detector side. The polarization of the excitation laser was changed using a half wave plate. A scrambler is placed after the analyzer to cancel out the errors due to polarization effects of the grating and the detector. The surface topography images of the  $\text{WS}_2$  coated Si/SiO<sub>2</sub> substrate were generated by the AFM (NX10 Park) system. For transmission measurements, a tapered fiber with a waist diameter of  $\sim 2 \text{ }\mu\text{m}$  was used to couple the light in and out of the resonator. One end of the tapered fiber is connected to the tunable laser source (Agilent 81600B, with tuning range from 1440 to 1640 nm) and the other end was connected to a power meter. The tapered fiber was coupled to the center of the MBR with the help of micro-positioning stages. The experimental arrangement for the light coupling with the MBR is shown in figure 3(B). Transmission measurements were done both before and after the coating of  $\text{WS}_2$  on the MBRs to check their Q-factors. The measurements were done with a step size of 0.1 pm.

### 3. Results and discussion

#### 3.1. Characterization of $\text{WS}_2$

**3.1.1. Determination of the number of layers of  $\text{WS}_2$ .** The first order optical modes of  $\text{WS}_2$  are denoted by  $\text{E}_{12g}^1$  and  $\text{A}_{1g}$ . Raman spectra of different layered samples of  $\text{WS}_2$  on fused silica substrates were recorded as shown in figure 4(A). According to Liang *et al* [12], the frequency difference between the  $\text{A}_{1g}$  and  $\text{E}_{12g}^1$   $\text{WS}_2$  peak points with monolayer and bi-layer are 60.31 and 62.18  $\text{cm}^{-1}$ , respectively; on the other hand for three and four layers it is 63.13 and 63.50  $\text{cm}^{-1}$ , respectively. Table 1 gives the data of the number of layer determination of the samples used in the present study.

The PL spectra were recorded for the identical exposure time of the excitation laser as a function of the  $\text{WS}_2$  layers (figure 4(B)). It can be seen that the PL intensity decreases for the multi-layered sample. Moreover, the spectrum shows a red-shift on increasing the layer number. With conformal coating of VdWE-grown  $\text{WS}_2$ , the majority of  $\text{WS}_2$  were bi-layer with a few layer  $\text{WS}_2$  flakes on the reference sample. The AFM images recorded for few layered  $\text{WS}_2$  shows triangular flakes

(figure 4(C)) with a height of  $\sim 6 \text{ nm}$  (figure 4(D)). The monolayer  $\text{WS}_2$  has a thickness of 0.8 nm indicating that the sample has  $\sim 7$  layers.

**3.1.2. Polarization dependent Raman spectra of  $\text{WS}_2$  coated MBR.** The Raman signal of  $\text{WS}_2$  coated MBR was studied as a function of the polarization angle of the incident beam. Figure 5 shows the Raman intensity at the polar angles of  $0^\circ$  and  $100^\circ$  (figure 5(A)) and  $0^\circ$  and  $180^\circ$  (figure 5(B)) respectively of the excitation laser. The intensity of the  $\text{E}_{12g}^1$  and  $\text{A}_{1g}$  modes at  $0^\circ$  has been denoted by  $I_{E0}$  and  $I_{A0}$ , respectively. The intensity ratio of the modes at different angles to that at  $0^\circ$  has been plotted as a function of the polarization angle and is shown in figure 5(C). It was observed that although the intensity ratio of the  $\text{E}_{12g}^1$  mode is almost constant (curve b), the  $\text{A}_{1g}$  mode ratio shows an oscillating feature (curve a). The ratio between  $\text{A}_{1g}$  mode and  $\text{E}_{12g}^1$  mode as a function of the polarization angle is shown in figure 5(D). It is noted that for the incoming ( $\varepsilon_i$ ) and outgoing polarization ( $\varepsilon_o$ ) the Raman cross section ( $\alpha \sum_i |\varepsilon_{0i} R_j \varepsilon_i|^2$ ;  $\alpha$  being a constant) is finite for OC modes but zero for IMC modes. Here, the incoming and outgoing lights are assumed to have the same helicity. The polarization state of the scattered photon can be obtained from the value of  $R_j$  which denotes the appropriate Raman tensor [13, 30]. The Raman tensors for  $\text{A}_{1g}$  and  $\text{E}_{12g}^1$  mode are given by

$$R_{A_{1g}} = \begin{pmatrix} a & 0 & 0 \\ 0 & a & 0 \\ 0 & 0 & b \end{pmatrix} \text{ and } R_{E_{12g}^1} = \begin{pmatrix} 0 & d & 0 \\ d & 0 & 0 \\ 0 & 0 & 0 \end{pmatrix}.$$

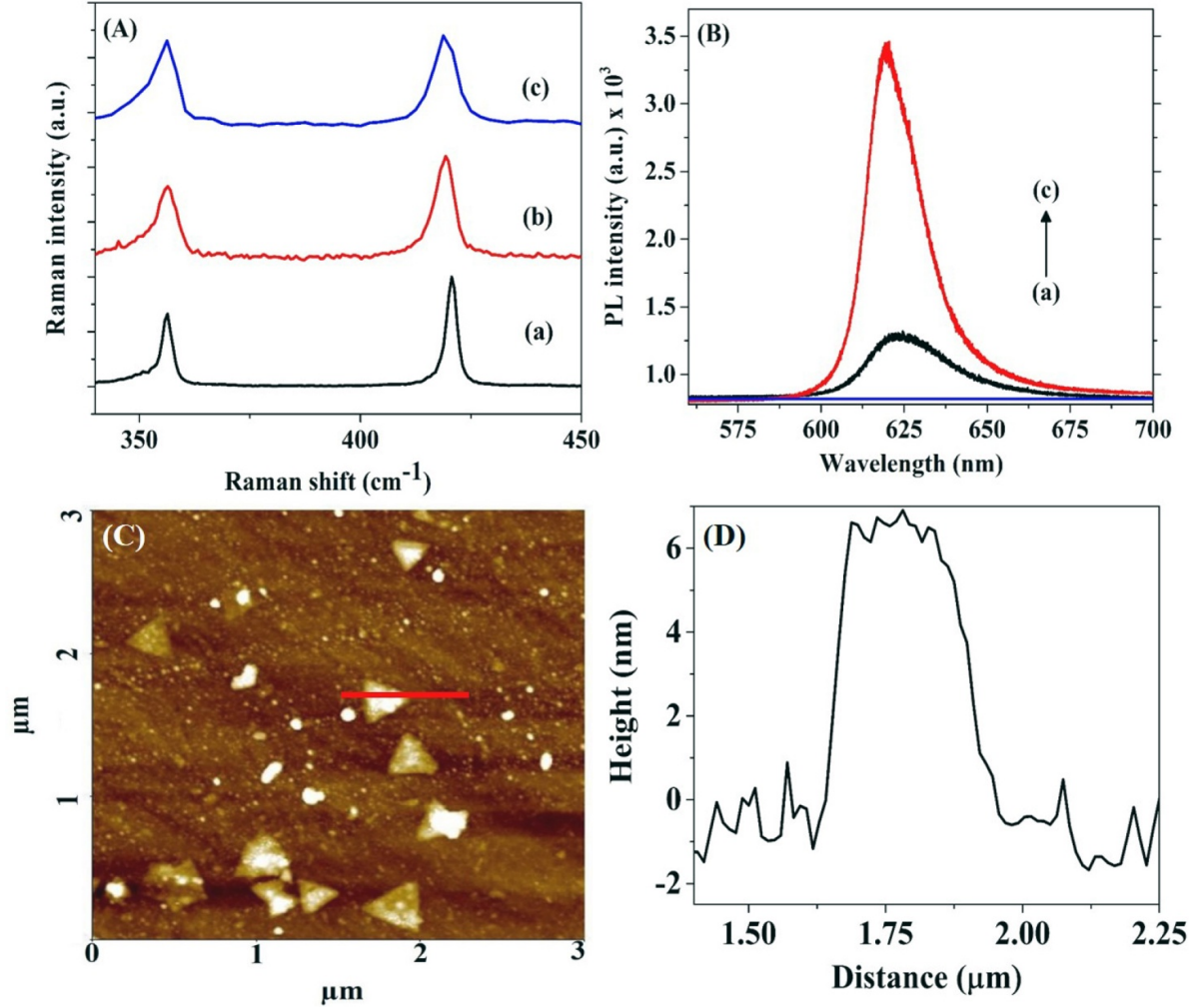
The value  $\langle \varepsilon_o | R_j | \varepsilon_i \rangle$  can be found to be equal to  $a$  (for  $\text{A}_{1g}$  mode) and zero (for  $\text{E}_{12g}^1$  mode) and thus the OC modes have the effect of polarization to the incident light. It is to be noted that the Raman intensities for the  $\text{A}_{1g}$  is  $\propto (a \cos^2 \theta + b \sin^2 \theta)$  where  $\theta$  is the input polarization of the laser and  $a, b$  are proportionality constants [31] and Raman intensity of  $\text{E}_{12g}^1$  mode is independent of polarization of laser [32]. Some variation in the intensity ratio of the  $\text{E}_{12g}^1$  can be observed in figure 5(C). This is because the optics does not have similar reflectivity in the s- and p-polarized states and these change with respect to  $\theta$  [31]. The intensity ratio feature of the  $\text{A}_{1g}$  mode with respect to the polarization angle is similar to that obtained for Si wafer [33]. Thus, the independence of the  $\text{E}_{12g}^1$  mode to the polarization of the excitation laser can also be used for identification of the material  $\text{WS}_2$ .

#### 3.2. Influence of coating of few layered $\text{WS}_2$ on the MBR

**3.2.1. Characterization of the MBR.** The characterization of the MBR was done before and after its coating with  $\text{WS}_2$  to determine the Q-factor of the WGMs (figure 6(A)). The transmission spectra exhibit groups of sharp resonance dips corresponding to the same azimuthal quantum number. The Q-factors were determined by fitting a Lorentzian function to the WGM as shown in figures 6(B) and (C). The value of  $Q$  is given as the ratio of the

**Table 1.** Obtained frequencies, frequency difference ( $\Delta\nu$ ) for the Raman modes and their intensity ratios ( $\lambda_{ex} = 488$  nm).

Phonon modes	Raman shift $\pm 1$ cm <sup>-1</sup>	$\Delta\nu$ cm <sup>-1</sup>	Intensity ratio ( $I_{A_{1g}}/I_{E_{2g}^1}$ )	No. of layers
$A_{1g}$ (cm <sup>-1</sup> ) $E_{2g}^1$ (cm <sup>-1</sup> )	418 356	62	0.95	2
$A_{1g}$ (cm <sup>-1</sup> ) $E_{2g}^1$ (cm <sup>-1</sup> )	419 356	63	0.73	3
$A_{1g}$ (cm <sup>-1</sup> ) $E_{2g}^1$ (cm <sup>-1</sup> )	419 354	65	0.45	Few layered

**Figure 4.** (A) Raman spectra for WS<sub>2</sub> on silica substrate for different number of layers: (a) few-layered, (b) bi-layer and (c) tri-layer WS<sub>2</sub>. (B) PL spectra of (a) few-layered (>3 layers), (b) tri-layer, and (c) bi-layered WS<sub>2</sub> respectively. (C) The AFM image of few-layered sample and (D) The height profile of one of the triangular flakes.

peak wavelength ( $\lambda_0$ ) of the mode to its full width at half maximum ( $\Delta\lambda$ ).

The total Q-factor ( $Q_{tot}$ ) of a microresonator strongly depends on the material losses ( $Q_{mat}^{-1}$ ) and the scattering losses due to surface roughness of the resonator ( $Q_{scat}^{-1}$ ) and can be written as  $\frac{1}{Q_{tot}} = \frac{1}{Q_{mat}} + \frac{1}{Q_{rad}} + \frac{1}{Q_{scat}}$  where  $Q_{rad}^{-1}$  is the radiation loss due to the curvature of the microresonator corresponding to the intrinsic quality factor. The modes in MBR are called higher order axial modes (bottle modes). The bottle modes are the result of broken degeneracy between WGMs with same azimuthal but different axial mode numbers. The free spectral range in MBRs are an order of magnitude smaller than that of microspheres of equal diameter [19] and are highly tunable.

These dense modes cause complications when MBRs are to be used for refractometry sensing.

The property of introducing the effect of scattering Q-factor can be used to attenuate some of the modes in an MBR. The coated MBR has a Q-factor  $\sim 10^5$  in contrast to its uncoated counterpart with a corresponding value of  $\sim 10^7$ . Although there is a significant decrease in the Q-factor by two orders of magnitude, well separated modes in the transmission spectrum are observed. Thus, by coating few layer WS<sub>2</sub> on the MBR a cleaner spectrum can be obtained (figure 6(A)). The decrease in Q-factor is due to the overlap of Mie scattering of atomically thin WS<sub>2</sub> layer with the WGMs of the MBR at 1550 nm.

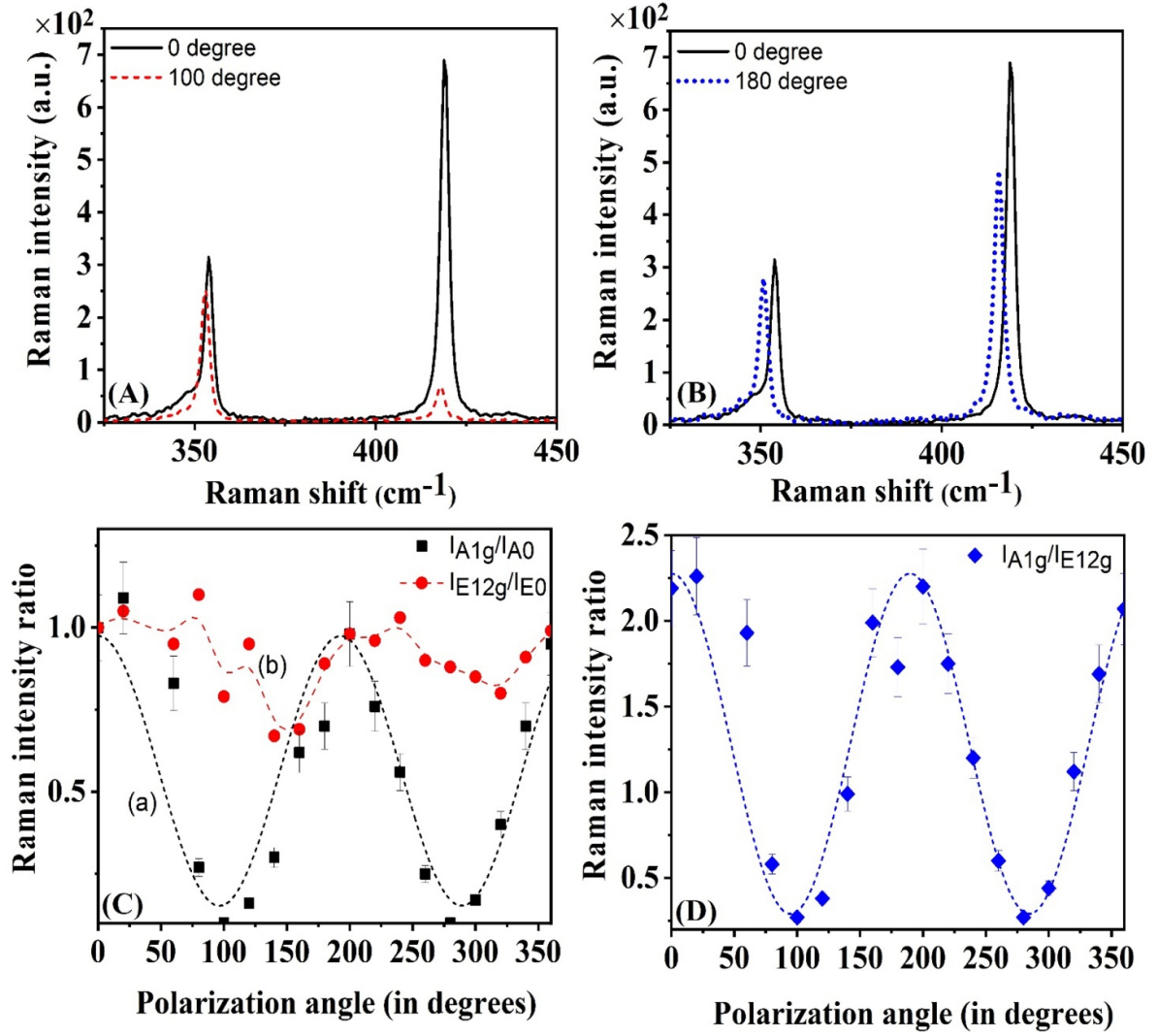


**Figure 5.** Intensity of the Raman modes as a function of the polarizer angle ( $0^\circ$ ,  $100^\circ$ ) (A) and ( $0^\circ$ ,  $180^\circ$ ) (B). (C) The intensity ratio for  $A_{1g}$ , (a) and  $E_{12g}$  (b) with respect to the intensity at  $0^\circ$  at various polarization angles. The fitted sine squared function is also given (---) for the case of  $A_{1g}$  mode. The dashed line in  $E_{12g}$  mode is simple spline connecting the measured data for guide to eye. (D) The intensity ratio between the  $A_{1g}$  and  $E_{12g}$  modes at various polarization angles with experimental results (◆) and sine squared fit to the data (---).

**3.2.2. Observation of Fano resonances.** Figure 7 shows a portion of the cleaned spectrum with high resolution scan of the coated MBR. The transmission spectrum (A) shows series of dips of varying shapes. For example, the symmetrical peak (peak II) fits to the EIT profile as shown in figure 7(B) while the asymmetrical dip (dip III) fits with the Fano type resonance (figure 7(C)). Fitting a spectral line with Fano formula can be a conclusive test for the observed Fano resonances [34]. Resonance III has an asymmetrical line profile and can be fitted to the Fano line shape (equation (1)). The Fano resonances in a MBR is given by [35]

$$T_{Fano} = T' + H' \frac{\left(1 + \frac{\lambda - \lambda_0}{sw}\right)^2}{1 + \left(\frac{\lambda - \lambda_0}{sw}\right)^2} \quad (1)$$

where  $T(\lambda)$  is the transmission at wavelength  $\lambda$ ,  $T'$  is a constant,  $H'$  is the amplitude,  $\lambda_0$  is the resonance wavelength,  $w$  is the width and  $s$  is the Fano asymmetry parameter. Fano resonance is the interference between a resonant scattering process and background. In general, in a typical tapered-fiber coupled WGM microresonator, the transmission profile consists of series of repetitive dips, which are Lorentzian-a state for the system. To produce a Fano-type line shape, we need another state- discrete or continuum to couple with the WGMs. The discrete state can be produced by introducing another WGM with a higher Q-factor [36] and also by coupling with a different resonator's mode by a waveguide [37]. Fano resonances were observed in a self-assembled MBR [35].  $WS_2$  does not have absorption in the 1500 nm regime. So, the decrease in Q-factor and appearance of different line shapes can be attributed to Mie scattering of the

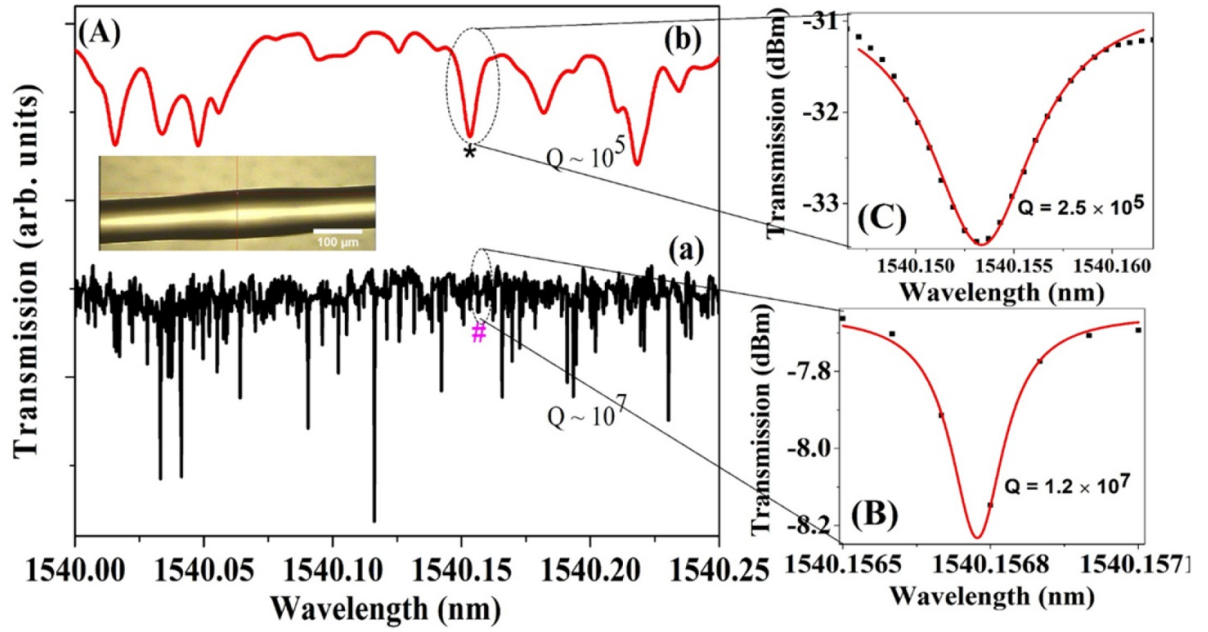


**Figure 6.** (A) Observed WGMs of MBR (a) before coating and (b) after coating of few-layer WS<sub>2</sub>. Spectra have been offset for brevity of presentation. Inset shows the MBR with  $D_b = 102 \mu\text{m}$  and  $D_s = 88 \mu\text{m}$ . (B), (C) Lorentzian fit to the WGM modes indicated by # and \*.

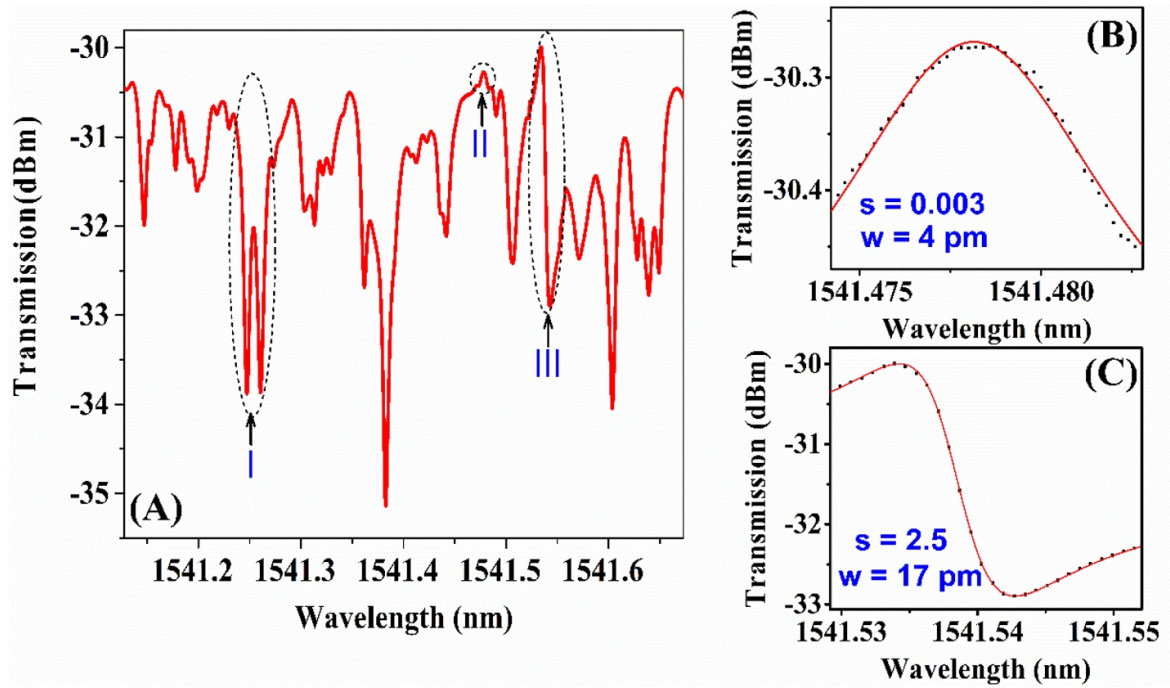


**Figure 7.** (A) observed WGMs of the coated MBR in high resolution scan. (B), (C) The close up of the resonance peaks II and III (....) and the fit with equation (1) (—).

atomically thin WS<sub>2</sub> layer which overlaps with the WGMs of the MBRs at 1550 nm. The transmission profile of the uncoated MBR shows symmetrical Lorentzian profiles confirming that the asymmetrical line shape appears due to the interference of the WGMs of the MBRs at 1550 nm and Mie scattering of WS<sub>2</sub>. Resonance II has an EIT-type line profile; the asymmetry parameter  $s$  has been found to be

0.003. The transparency window in EIT has been found to be 0.001 nm.

**3.2.3. Autler Townes splitting.** It was observed that the spectrum has features of mode splitting. This is a feature of strong coupling. Some of the resonance modes in the transmission

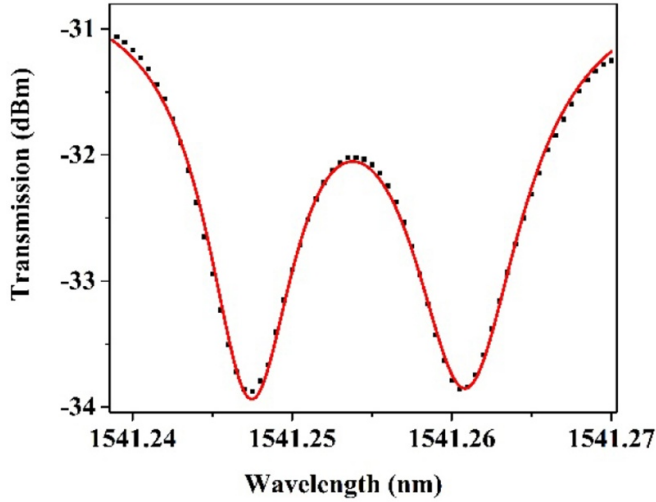


**Figure 8.** ATS in the transmission spectrum of the MBR (peak I as indicated in figure 7(A)). The solid curve shows the fit with the ATS profile (equation (2)).

profile split into two associated modes thus giving rise to a transparency window in between.

For example, the resonance I (figure 7(A)) shows two associated dips in the transmission spectrum. This resonance can be fitted with AT type of splitting (figure 8).

The resonance mode (I) in the transmission profile splits into a symmetric doublet and gives rise to a wide transparency window. The transmission of ATS has the contribution of two Lorentzian profiles as given by [38]

$$T_{ATS}(\lambda) = T'' + C_1 \frac{\Gamma/2}{(\lambda - \lambda_c)^2 + (\frac{\Gamma}{2})^2} + C_2 \frac{\Gamma/2}{(\lambda + \lambda_c)^2 + (\frac{\Gamma}{2})^2} \quad (2)$$

where  $T''$ ,  $\Gamma$  are constants and  $\lambda_c$  is the center wavelength. As shown in figure 8, the profile has been fitted with equation (2) and the Q factors for the adjacent pair of modes are found to be  $Q_1 = 2.3 \times 10^5$ ,  $Q_2 = 1.8 \times 10^5$ . The effects of ATS in the transmission profile is similar to EIT as they both display a transparency window, i.e. reduction in the absorption spectrum. The transparency window has been found to be 0.013 nm which is an order of magnitude wider than transparency window observed in EIT (0.001 nm) similar to that reported in literature [39]. Here ATS may originate due to lifting of the frequency degeneracy of the eigenmodes, thereby splitting into two resonances due to strong tapered fiber-MBR coupling.

The coherent interaction of the scattering modes of the WS<sub>2</sub> flakes and WGMs of the microcavity can lead to the asymmetric line profile and splitting [40, 41]. In order to estimate scattering mode spectrum of the WS<sub>2</sub> flakes, we performed FEM simulations in which the triangular WS<sub>2</sub> flakes with varying side lengths from 100 to 300 nm and a thickness of 6 nm, similar to that observed from the AFM data (figure 9) was simulated. The triangles have been taken to be equilateral. It can be observed that the scattering spectrum show maxima in the 1500–1700 nm range. A red shift is observed with the increase

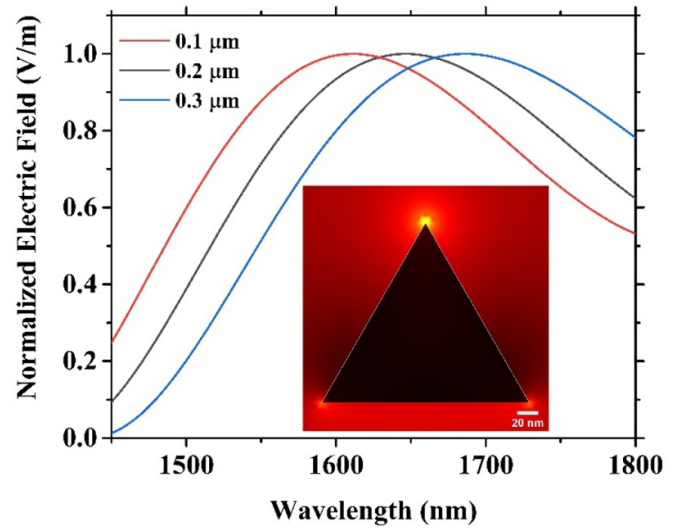


**Figure 9.** Scattered electric field spectra of different sizes of triangular WS<sub>2</sub> flakes. Inset shows the hotspots at the apex of the triangle.

in length of the flakes. WS<sub>2</sub> does not have absorption in the 1550 nm regime [42]. Hence, the decrease in Q-factor and appearance of different line shapes can be attributed to Mie scattering of the atomically thin WS<sub>2</sub> layer which overlaps with the WGMs of the MBRs at 1550 nm. Since Fano profiles are not observed for the WGMs of the uncoated spectrum, it can be concluded that the appearance of these asymmetric profiles is due to the coherent interaction of the scattering E-field of the WS<sub>2</sub> flakes with the MBRs WGMs already present at 1550 nm.

#### 4. Conclusions

A few layered films of the TMDC material WS<sub>2</sub> have been fabricated on a fused silica substrate and MBR by VdWE method. The number of layers have been determined by using the Raman spectroscopy. The A<sub>1g</sub> Raman mode of the sample shows polarization dependence of the excitation light. WGMs were observed in the transmission spectrum of the uncoated and WS<sub>2</sub>-coated MBR. The Q-factor of few-layer WS<sub>2</sub>-coated MBR decreases by two orders of magnitude as compared to that of the uncoated MBR. The coated MBR shows a cleaned spectrum with specific WGM resonances. The WGMs now exhibit resonance dips and peaks that fit with Fano-like asymmetric resonance and ATS, a feature of strong-coupling regime. Simulations show that the Fano resonances appear because of the interference of the WGMs at 1550 nm and Mie scattering of the WS<sub>2</sub> flakes. It is expected that the Fano resonances can be tuned by variation of the layer number of the TMDC material.

The integration of TMDC to a microresonator have prospects in device applications including low threshold microlasing, enhanced Raman sensing and strong light–matter interaction with associated nonlinear effects. The resonance spectrum of a coated MBR is much cleaner with well-defined peaks,

which is essential for sensing applications. If required, the Q-factors can be controlled by (a) allowing only few nanocrystals to grow on the microresonator, which will decrease both scattering losses and material absorption and (b) by growing a more uniform coating on the resonators to reduce the scattering losses.

## Acknowledgments


The authors thank Department of Science and Technology (DST) for financial support. We also thank EU FP7 Grant Agreement No. 318941 under the project ‘Ultrafast Photonics-Processes and Interactions (UP-PI)’ for travel funds. The 2D materials work is partly funded through the Future Photonics Manufacturing Hub (EPSRC EP/N00762X/1) and the Chalcogenide Photonic Technologies (EPSRC EP/M008487/1) at University of Southampton, United Kingdom.

## ORCID iDs

Shubhayan Bhattacharya  <https://orcid.org/0000-0003-0085-9870>

Aneesh V Veluthandath  <https://orcid.org/0000-0003-4306-6723>

C C Huang  <https://orcid.org/0000-0003-3471-2463>

Ganapathy Senthil Murugan  <https://orcid.org/0000-0002-2733-3273>

Prem B Bisht  <https://orcid.org/0000-0002-5643-6685>

## References

- [1] Novoselov K S, Geim A K, Morozov S V, Jiang D, Zhang Y, Dubonos S V, Grigorieva I V and Firsov A A 2004 Electric field effect in atomically thin carbon films *Science* **306** 666–9
- [2] Ansari N and Ghorbani F 2018 Light absorption optimization in two-dimensional transition metal dichalcogenide van der Waals heterostructures *J. Opt. Soc. Am. B* **35** 1179–85
- [3] Mak K F, Lee C, Hone J, Shan J and Heinz T F 2010 Atomically thin MoS<sub>2</sub>: a new direct-gap semiconductor *Phys. Rev. Lett.* **105** 2–5
- [4] Xia F, Wang H, Xiao D, Dubey M and Ramasubramanian A 2014 Two-dimensional material nanophotonics *Nat. Photon.* **8** 899–907
- [5] Shim J, Park H-Y, Kang D-H, Kim J-O, Jo S-H, Park Y and Park J-H 2017 Electronic and optoelectronic devices based on two-dimensional materials: from fabrication to application *Adv. Electron. Mater.* **3** 1600364
- [6] Ye Y, Wong Z J, Lu X, Ni X, Zhu H, Chen X, Wang Y and Zhang X 2015 Monolayer excitonic laser *Nat. Photon.* **9** 733–7
- [7] Veluthandath A V and Bisht P B 2017 Identification of whispering gallery mode (WGM) coupled photoluminescence and Raman modes in complex spectra of MoS<sub>2</sub> in polymethyl methacrylate (PMMA) microspheres *J. Lumin.* **187** 255–9
- [8] Schneider C, Glazov M M, Korn T, Höfling S and Urbaszek B 2018 Two-dimensional semiconductors in the regime of strong light-matter coupling *Nat. Commun.* **9** 2695
- [9] Baranov D G, Wersäll M, Cuadra J, Antosiewicz T J and Shegai T 2018 Novel nanostructures and materials for strong light-matter interactions *ACS Photonics* **5** 24–42
- [10] Das S, Robinson J A, Dubey M, Terrones H and Terrones M 2015 Beyond graphene: progress in novel two-dimensional materials and van der Waals solids *Annu. Rev. Mater. Res.* **45** 1–27
- [11] Kern J et al 2015 Nanoantenna-enhanced light-matter interaction in atomically thin WS<sub>2</sub> *ACS Photonics* **2** 1260–5
- [12] Liang L and Meunier V 2014 First-principles Raman spectra of MoS<sub>2</sub>, WS<sub>2</sub> and their heterostructures *Nanoscale* **6** 5394
- [13] Chen S-Y, Zheng C, Fuhrer M S and Yan J 2015 Helicity-resolved Raman scattering of MoS<sub>2</sub>, MoSe<sub>2</sub>, WS<sub>2</sub>, and WSe<sub>2</sub> atomic layers *Nano Lett.* **15** 2526–32
- [14] Liu X, Bao W, Li Q, Ropp C, Wang Y and Zhang X 2017 Control of coherently coupled exciton polaritons in monolayer tungsten disulphide *Phys. Rev. Lett.* **119** 027403
- [15] Chiasera A, Dumeige Y, Féron P, Ferrari M, Jestin Y, Conti G N, Pelli S, Soria S and Righini G C 2010 Spherical whispering-gallery-mode microresonators *Laser Photonics Rev.* **4** 457–82
- [16] Bhattacharya S, Veluthandath A V and Bisht P B 2018 Whispering gallery modes in photoluminescence of ruthenium bipyridine in coated microcavities *Mater. Res. Express* **5** 1–12
- [17] Ganta D, Dale E B, Rezac J P and Rosenberger A T 2011 Optical method for measuring thermal accommodation coefficients using a whispering-gallery microresonator *J. Chem. Phys.* **135** 084313
- [18] Sandeep P and Bisht P B 2005 Effect of adsorbed concentration on the radiative rate enhancement of photoexcited molecules embedded in single microspheres *J. Chem. Phys.* **123** 204713
- [19] Murugan G S, Wilkinson J S and Zervas M N 2009 Selective excitation of whispering gallery modes in a novel bottle microresonator *Opt. Express* **17** 11916–25
- [20] Sumetsky M 2004 Whispering-gallery-bottle microcavities: the three-dimensional etalon *Opt. Lett.* **29** 8–10
- [21] Mohd Nasir M N, Senthil Murugan G and Zervas M N 2016 Spectral cleaning and output modal transformations in whispering-gallery-mode microresonators *J. Opt. Soc. Am. B* **33** 1963
- [22] Fano U 1961 Effects of integration on intensities and phase shifts *Phys. Rev.* **124** 1866–78
- [23] Tomita M, Totsuka K, Hanamura R and Matsumoto T 2009 Tunable Fano interference effect in coupled-microsphere resonator-induced transparency *J. Opt. Soc. Am. B* **26** 813–8
- [24] Luk'yanchuk B S, Miroshnichenko A E and Kivshar Y S 2013 Fano resonances and topological optics: an interplay of far- and near-field interference phenomena *J. Opt.* **15** 073001
- [25] Lukin M D, Fleischhauer M, Scully M O and Velichansky V L 1998 Intracavity electromagnetically induced transparency *Opt. Lett.* **23** 295–7
- [26] Ma L, Slattery O and Tang X 2017 Optical quantum memory based on electromagnetically induced transparency *J. Opt.* **19** 043001
- [27] Orsi Gordo V et al 2018 Revealing the nature of low temperature photoluminescence peaks by laser treatment in van der Waals epitaxially grown WS<sub>2</sub> monolayers *Nanoscale* **10** 4807–15
- [28] Felix J F, da Silva A F, da Silva S W, Qu F, Qiu B, Ren J, de Azevedo W M, Henini M and Huang C 2020 A comprehensive study on the effects of gamma radiation on the physical properties of a two-dimensional WS<sub>2</sub> monolayer semiconductor *Nanoscale Horiz.* **5** 259–67
- [29] Mlack J T et al 2017 Transfer of monolayer TMD WS<sub>2</sub> and Raman study of substrate effects *Sci. Rep.* **7** 43037
- [30] Loudon R 1964 The Raman effect in crystals *Adv. Phys.* **13** 423–82

- [31] Zobeiri H, Wang R, Deng C, Zhang Q and Wang X 2019 Polarized Raman of nanoscale two-dimensional materials: combined optical and structural effects *J. Phys. Chem. C* **123** 23236–45
- [32] Saito R, Tatsumi Y, Huang S, Ling X and Dresselhaus M S 2016 Raman spectroscopy of transition metal dichalcogenides *J. Phys.: Condens. Matter* **28** 353002
- [33] Yoo W S, Harima H and Yoshimoto M 2015 Polarized Raman signals from Si wafers: dependence of in-plane incident orientation of probing light *ECS J. Solid State Sci. Technol.* **4** 356–63
- [34] Limonov M F, Rybin M V, Poddubny A N and Kivshar Y S 2017 Fano resonances in photonics *Nat. Photon.* **11** 543–54
- [35] Veluthandath A V, Bhattacharya S, Murugan G S and Bisht P B 2019 Fano resonances and photoluminescence in self-assembled high-quality-factor microbottle resonators *IEEE Photonics Technol. Lett.* **31** 226–9
- [36] Li B B, Xiao Y-F, Zou C-L, Liu Y-C, Jiang X-F, Chen Y-L, Li Y and Gong Q 2011 Experimental observation of Fano resonance in a single whispering-gallery microresonator *Appl. Phys. Lett.* **98** 021116
- [37] Li B B, Xiao Y F, Zou C L, Jiang X F, Liu Y C, Sun F W, Li Y and Gong Q 2012 Experimental controlling of Fano resonance in indirectly coupled whispering-gallery microresonators *Appl. Phys. Lett.* **100** 021108
- [38] Peng B, Özdemir Ş K, Chen W, Nori F and Yang L 2014 What is and what is not electromagnetically induced transparency in whispering-gallery microcavities *Nat. Commun.* **5** 1–9
- [39] Li B, Ho C P and Lee C 2016 Tunable Autler–Townes splitting observation in coupled whispering gallery mode resonators *IEEE Photonics J.* **8** 1–10
- [40] Doleman H M, Verhagen E and Koenderink A F 2016 antenna–cavity hybrids: matching Polar opposites for Purcell enhancements at any linewidth *ACS Photonics* **3** 1943–51
- [41] Heylman K D, Thakkar N, Horak E H, Quillin S C, Cherqui C, Knapper K A, Masiello D J and Goldsmith R H 2016 Optical microresonators as single-particle absorption spectrometers *Nat. Photon.* **10** 788–95
- [42] Dong N, Li Y, Feng Y, Zhang S, Zhang X, Chang C, Fan J, Zhang L and Wang J 2015 Optical limiting and theoretical modelling of layered transition metal dichalcogenide nanosheets *Sci. Rep.* **5** 14646